RESEARCH ARTICLE

ADVANCED MATERIALS INTERFACES Open Access

www.advmatinterfaces.de

Interface Engineering and Oxygen Vacancy Control in $SrTiO_3$-TiO_2 Eutectics

Zhiwei Hou, Yefei Guo, Hafiz Muhammad Zeeshan, Elena Voloshina,* and Yuriy Dedkov**

The development of highly efficient semiconducting materials is essential for achieving the high-yield and stable hydrogen and/or oxygen evolution reactions (HER/OER) in photoelectrochemical (PEC) water splitting reactions. The $SrTiO_3$-TiO_2 eutectic compound has recently emerged as a perspective material with extraordinary activities in the PEC field due to the unique crystallographic and electronic properties caused by the large number of oxygen vacancies in the bulk. In the present study, different experimental techniques (XPS, SEM/EDX, TEM/EDX) are used to provide a detailed investigation of the changes in the structural and electronic properties of the $SrTiO_3$-TiO_2 eutectic upon annealing under various gaseous environments (in vacuum, air, oxygen, argon). These results demonstrate that thermal annealing in different environments significantly enhances the formation of a sharp interface between the two crystalline phases and allows to control the concentration of the oxygen vacancies within the eutectic material.

1. Introduction

Solar water splitting holds significant promise for harnessing and storing abundant renewable sunlight energy on Earth. In the field of photochemical (PC) or photoelectrochemical (PEC) water splitting, semiconductor materials have been extensively employed as photocatalysts or photoanodes to efficiently absorb sunlight and facilitate the transfer of solar energy into chemical states.[1,2] In recent decades, considerable research efforts have been dedicated to investigation of numerous candidate materials, such as TiO_2,[3,4] $SrTiO_3$,[5] ZnO,[6,7] C_3N_4,[8] transition metal di– and trichalcogenides[9–13] and many others, in order to achieve economically and energetically efficient PC or PEC water splitting.

Among these semiconductors, TiO_2 and $SrTiO_3$ have emerged as representative materials in PEC systems for the hydrogen (H_2) generation via water-splitting reactions, owing to their remarkable efficiency, cost–effectiveness, and robustness. The application of TiO_2 in this role was reported for the first time in 1972,[14,15] followed by $SrTiO_3$ in 1980.[16,17] Moreover, composite oxides, e.g., in the form of the so-called eutectic materials, have gained significant attention as photoanode and photocatalytic materials in PEC systems.[18] Such eutectic composites, particularly, offer distinct advantages for solar energy conversion, characterized by highly ordered structures and well-defined interfaces between phases. In the later study, the $SrTiO_3$-TiO_2 (STO-TO) eutectic, a representative example of such composites, was chosen as a focal point for drawing the perspectives of application of semiconducting eutectics in different catalytic applications. By exploring and comprehending the properties and performance of eutectic composites, like STO-TO, the aim is to develop more efficient and cost-effective materials for solar water splitting.

However, the practical application of TiO_2, $SrTiO_3$, and their composites are limited by their relatively wide band gaps (3.0 and 3.2 eV, respectively). To overcome this limitation and enhance the light absorption properties of these materials, various approaches have been explored, including element doping, dye sensitization, and the formation of coupled semiconductor compounds.[19–22] The deposition of noble metals has been found to serve as electron traps, effectively inhibiting the recombination rate of charge carriers.[23,24] Furthermore, the surface plasmon resonance (SPR) effect exhibited by noble metals has been utilized to enhance the light absorption and improve the photocatalytic activity.[25] Non-metal and transition metal doping have been employed to extend the light absorption range to the visible part of the spectrum

Z. Hou, Y. Guo
School of Physics and Advanced Energy
Henan University of Technology
Zhengzhou, Henan 450000, P. R. China
E-mail: yefeiguo@haut.edu.cn

H. M. Zeeshan
Institute of Chemical Reaction Engineering
Hamburg University of Technology (TUHH)
Eißendorfer Straße 38, 21073 Hamburg, Germany

E. Voloshina
Division of Theoretical Physics
Ruđer Bošković Institute
Bijenička cesta 54, Zagreb 10000, Croatia
E-mail: elena.voloshina@irb.hr

Y. Dedkov
Center for Advanced Laser Techniques
Institute of Physics
Bijenička 46, Zagreb 10000, Croatia
E-mail: ydedkov@ifs.hr

The ORCID identification number(s) for the author(s) of this article can be found under https://doi.org/10.1002/admi.202500911

DOI: 10.1002/admi.202500911

and suppress electron–hole recombination, respectively.[26,27] Additionally, dye sensitization has proven to be effective in enhancing visible light absorption, while coupled semiconductor structures have been employed to facilitate charge carrier separation and broaden the overall light absorption spectrum.[28,29]

In addition to the aforementioned strategies, the defects' engineering in semiconducting materials has been recognized as an effective approach for enhancing the photoelectrochemical (PEC) performance of the STO-TO eutectic and other oxides.[30–33] Theoretical calculations and experimental investigations have provided evidence that oxygen defects, specifically oxygen vacancies (O_V), can function as shallow donors and active sites for surface reactions.[34,35] The presence of oxygen vacancies on the surface of the STO-TO eutectic brings changes in its electronic structure and chemical properties, making the introduction of oxygen vacancies a crucial factor in modifying the physical and chemical characteristics of the eutectic composite. Various methods have been employed to introduce oxygen vacancies into STO-TO eutectics, including heating, hydrogenation,[36] ion implantation,[37] and light irradiation.[38] Among these methods, annealing has emerged as a widely utilized approach for promoting the formation of oxygen vacancies. For instance, Li et al.[39] successfully prepared oxygen-vacancy-contained TiO_2 (TiO_{2-x}) nanorod films by annealing TiO_2 samples under ultrahigh vacuum (UHV) conditions. Their study demonstrated that the introduction of oxygen vacancies through this method is a simple and effective way of enhancing the surface-enhanced Raman scattering (SERS) sensitivity in TiO_2. Similarly, Bi et al.[30] synthesized colored TiO_2 through facile calcination under different atmospheres (air, N_2, or Ar) and revealed the influence of annealing atmospheres on the oxygen vacancy content and photocatalytic performance of TiO_2. Additionally, Rao et al.[40] reported the emergence of robust ferromagnetism in undoped $SrTiO_3$ single crystals following laser annealing treatment, which was found to be primarily attributed to the presence of oxygen vacancies. As evident from the presented examples, oxygen defects play a crucial role in determining the physical and chemical properties of oxides. However, the influence of different annealing conditions on the electronic structure of the STO-TO eutectic composite has not yet been thoroughly explored in the literature.

Here, we report the systematic spectroscopic and microscopic studies of the electronic and crystallographic structure modifications of the semiconducting $SrTiO_3$-TiO_2 eutectic compound upon thermal annealing in different conditions. The elements' chemical states, morphological, and structural changes in STO-TO eutectic upon annealing were traced using X-ray photoelectron spectroscopy (XPS), scanning electron microscopy (SEM), and high-resolution transmission electron microscopy (HR-TEM) methods combined with energy-dispersive X-ray (EDX) analysis. Our XPS results demonstrate the increase of the number of oxygen vacancies upon stepwise annealing at the low and high pressures of gases (air, pure Ar, and O_2); however, different atmospheres have different inhibiting effects on the final content of oxygen vacancies. Moreover, the microscopic studies show the improved crystallographic order of the interface between two phases after annealing in high-pressure atmospheres. Interestingly, the SEM images indicate barely any changes in the surface morphology after annealing in UHV atmospheres. On the contrary to this, the obvious changes in the surface morphology after annealing at high pressure of gases can be observed due to the evaporation of Sr. Our research provides the clear evidence of the influence of different atmospheres on the electronic and crystallographic structures of the STO-TO eutectic. The presented findings contribute to the current understanding of the controllable modulation of oxygen vacancy concentrations, revealing the promising potential of the STO-TO eutectic for use for desired applications across various domains.

2. Results and Discussion

2.1. SEM/EDX Analysis

Figures 1 and **2** present the results of the SEM/EDX studies of the STO-TO eutectic samples "before" and "after" annealing at 1000 °C in vacuum conditions (UHV, and using different partial pressures of O_2 or Ar) and in atmospheric-pressure gas flows (air, Ar, or O_2), respectively. As we can see, the special surface morphology of $SrTiO_3$ and TiO_2 with a clear phase separation for the as-grown, as-cut, polished and freshly cleaned eutectic sample is observed in Figure 1a. Also, the elements' distribution map (insets of Figure 1d) indicates the darker TiO_2 phase and brighter $SrTiO_3$ phase of the eutectic compound in the SEM images, that is in line with the previously published data.[41,42] Figure 1b,c shows the surface morphology of the STO-TO eutectic after annealing in vacuum conditions at 1000 °C and partial pressure of 1×10^{-6} mbar for Ar and O_2, respectively. It can be seen that no obvious changes in the morphology are observed after thermal treatment in low-pressure conditions of the STO-TO samples. By observing the characteristic X-ray intensity data of the oxygen element obtained after EDX scanning of different regions (corresponding to the two phases of the eutectic compound) (Figure 1), it is found that the actually measured peak intensity of the oxygen element is significantly lower than that in the case of the ideal stoichiometric ratio, which directly indicates that the content of the oxygen element is relatively insufficient. The elements' EDX analysis demonstrate the large deficiency of oxygen in both phases of the eutectic compound explaining the black color of these samples, that is in agreement with previous work.[42] Further EDX analysis presented in **Table 1** shows that the oxygen concentration is decreased in both $SrTiO_3$ and TiO_2 phases upon thermal annealing, indicating that the oxygen atoms escaped from the lattice. Considering the two thermal treatments using Ar and O_2 one can find that the oxygen concentration in STO-TO eutectic after annealing in oxygen is slightly less compared to the one annealed in Ar.

The SEM images of STO-TO eutectic samples after annealing in the atmospheric-pressure flow of air or pure gases (Ar or O_2) show obvious changes in the surface morphologies (Figure 2a–c). Particularly, the surface of the TiO_2 phase with special rectangular shapes becomes more rough compared to the SEM results for the STO-TO sample before thermal treatment. The respective EDX curves collected for different areas of the sample are shown in Figure 2d–f. As can be seen from these results (Figure 2), which are also compiled in Table 1, there is the same trend for all samples after thermal treatment that almost all Sr for the regions corresponding to the $SrTiO_3$ phase have almost disappeared. Additionally, according to the same results presented in Table 1 for the thermal treatment in the atmospheric-pressure

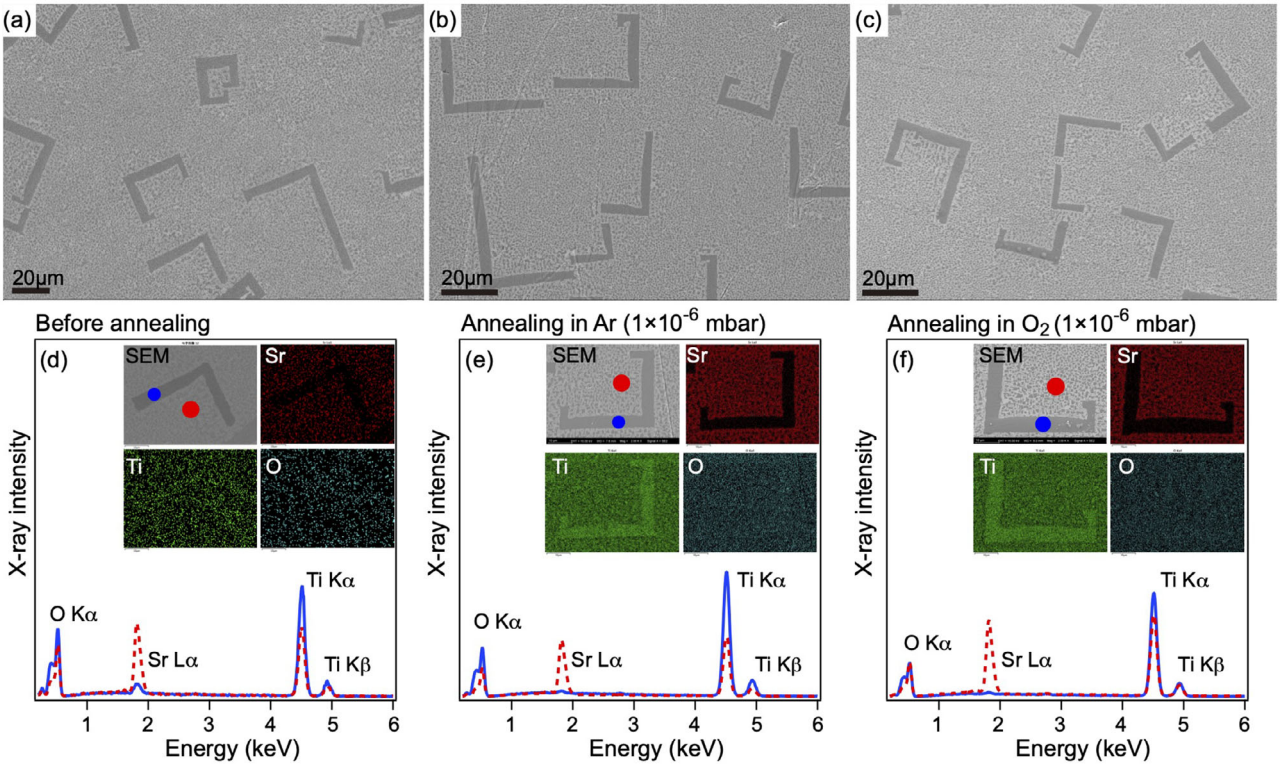

Figure 1. a–c) SEM images of $SrTiO_3$-TiO_2 eutectic collected "before" and "after" annealing at 1000 °C in Ar (1×10^{-6} mbar) and O_2 (1×10^{-6} mbar), respectively. d–f) The corresponding SEM/EDX data. Insets show the respective EDX maps.

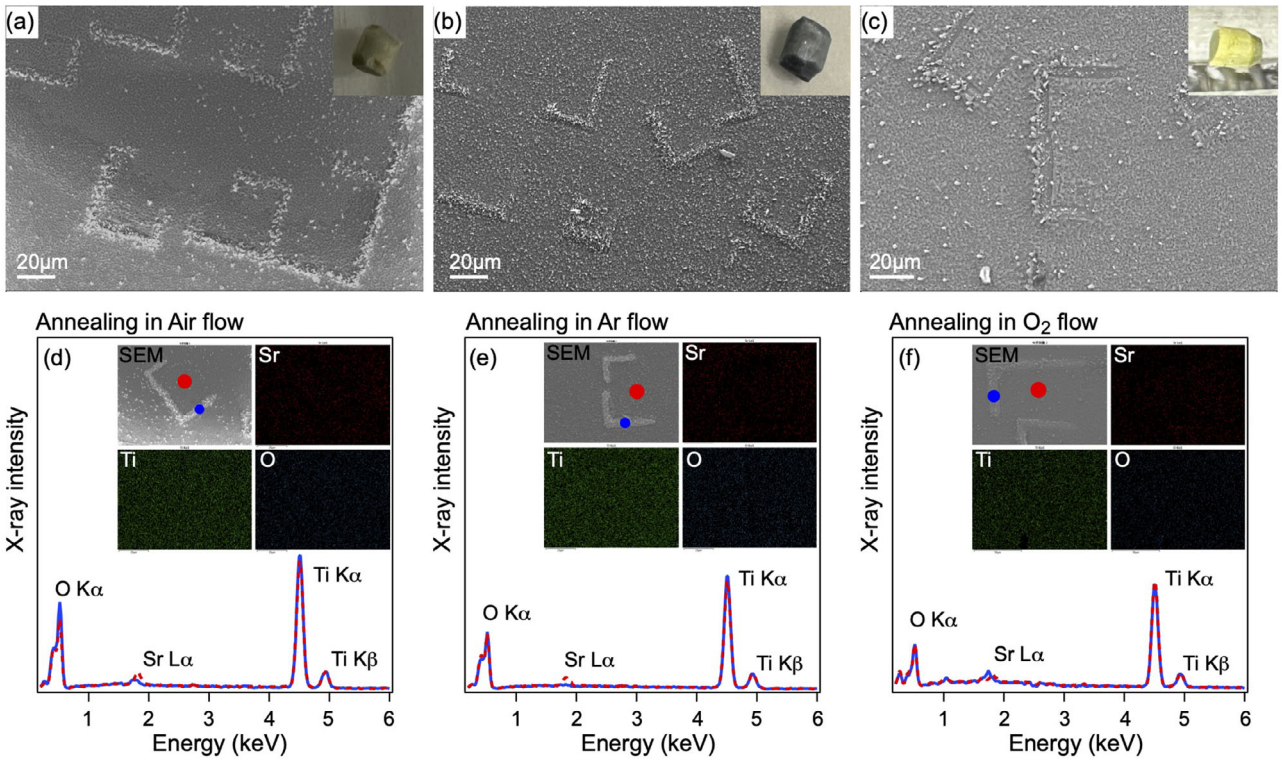

Figure 2. a–c) SEM images of $SrTiO_3$-TiO_2 eutectic collected "after" annealing at 1000° C in the flow of air, Ar, and O_2, respectively. Insets show photos of obtained samples. d–f) The corresponding SEM/EDX data. Insets show the respective EDX maps.

Table 1. Atomic concentrations (%) as extracted from SEM/EDX data for the STO-TO sample "before" and "after" thermal annealing in different conditions.

	Before	Ar [1×10^{-6} mbar]	O_2 [1×10^{-6} mbar]	Air flow	Ar flow	O_2 flow
$SrTiO_3$						
Sr	38.1	36.86	38.82	6.16	4.64	7.34
Ti	39.3	46.71	47.16	61.84	64.38	68.62
O	22.6	16.43	14.02	32.00	30.98	24.04
TiO_2						
Sr	5.5	3.1	1.43	3.32	2.21	7.41
Ti	60.5	70.49	74.66	61.24	66.71	69.30
O	34.0	26.41	23.91	35.44	31.08	23.29

flow of air or pure gases, we can draw the same conclusion that the oxygen concentration in STO-TO after annealing in O_2 in both $SrTiO_3$ and TiO_2 phases is slightly lower compared to treatment in other gases.

2.2. TEM/EDX Analysis

Our previous X-ray diffraction and HR-TEM studies demonstrate that the crystallographic order of the eutectic STO-TO compounds is significantly improved after their thermal annealing in UHV conditions.[42] In order to study the effect of the Sr disappearance from the surface of the STO-TO eutectic observed in SEM/EDX as well as the influence of the simultaneous "high-pressure" and high-temperature treatments of these materials we performed the combined high-resolution TEM/EDX studies. These results are presented in **Figure 3**. As shown, the STO-TO eutectic material before thermal treatment is characterized by a less ordered structure compared to the state examined after annealing in the flow of pure gases. This can be clearly observed from the HR-TEM image and the respective Fast Fourier Transformation (FFT) patterns for this interface (Figure 3a). The fuzzy background and the fewer spots in the diffraction ring observed in the FFT image is a sign of the lower crystallographic order. Notably, the interface between TiO_2 and $SrTiO_3$ phases is quite blurry and extended over several nms, combining structures from two components of the eutectic material. For the STO-TO samples obtained after the high-temperature annealing in the flow of gases, the clear and sharp interfaces between TiO_2 and $SrTiO_3$ phases are observed (Figure 3b–d). This demonstrates the improved crystallographic order of the $SrTiO_3$-TiO_2 eutectic after the thermal treatment. As it is known, the sharp interface and

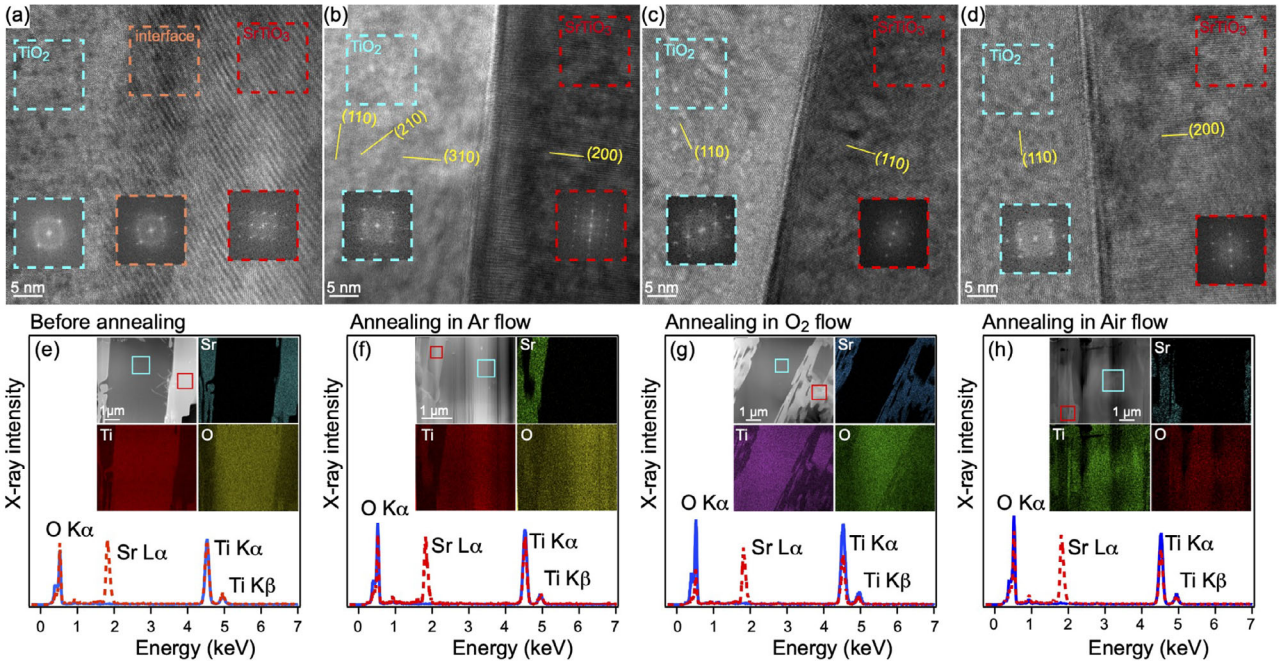

Figure 3. a–d) High-resolution TEM images of the interface region between TiO_2 (left) and $SrTiO_3$ (right) phases and collected "before" and "after" annealing of eutectic samples in Ar, O_2, and air flow. Insets show the respective FFT images. e–h) The corresponding SEM/EDX data. Insets show the respective EDX maps.

Table 2. Atomic concentrations (%) as extracted from TEM/EDX data for the STO-TO sample "before" and "after" thermal annealing in different conditions.

	"Before"	Ar flow	O_2 flow	Air flow
$SrTiO_3$				
Sr	30.80	32.83	38.33	37.61
Ti	30.42	41.62	44.38	33.29
O	38.78	25.55	17.29	29.10
TiO_2				
Sr	0.15	0.46	0.37	0.78
Ti	46.01	57.88	59.92	53.07
O	53.84	41.66	39.71	46.15

the high crystallinity of the eutectic compound can enhance the electrical contact between two phases, leading to higher charge carriers' mobilities that might lead to the higher performance in the photoelectrochemical water splitting reactions.[43]

The respective TEM/EDX data for the STO-TO samples collected before and after thermal treatment in the flow of gases are shown in Figure 3e–h and the corresponding extracted elements' concentrations are summarized in **Table 2**. According to the elemental distribution maps, we can find that Sr inside the eutectic compound survived the high-temperature annealing in the flow of different gases at 1000 °C. Comparison of the obtained atomic concentrations for oxygen in the obtained TEM/EDX data and in the previously presented SEM/EDX results, suggests that independent on the "low-pressure" or "high-pressure" annealing conditions, oxygen will leave the STO-TO compound. Thus, we can conclude that probably the much higher gas pressures are required for the oxygen-vacancies compensation in the STO-TO eutectic compounds.

2.3. XPS Analysis

2.3.1. Low-Pressure Treatment

In order to further elucidate the role of oxygen vacancies in the electronic structure of the STO-TO materials, the systematic XPS studies of these compounds were performed as a function of the annealing temperature and for the "low-pressure" and "high-pressure" treatments using different gases. These results are summarized in **Figures 4–6** and Figures S1–S8 (Supporting Information) of, respectively. Here, the main text figures present the results "before" (in the beginning of the thermal treatment) and "after" the final thermal annealing step at 1000 °C, while Supplementary Information presents all XPS data and the respective treatment collected during the stepwise thermal annealing in different gaseous environments.

Figure 4 presents the XPS results for the STO-TO eutectic during thermal treatment in O_2 at a partial pressure of 1×10^{-8} and 1×10^{-6} mbar, respectively (see also, Figures S2 and S3, Supporting Information of). The presented survey XPS spectra (Figures S2 and S3, Supporting Information) show the presence of all elements from the STO-TO samples during thermal annealing procedure. As can be seen from these spectra, after annealing step at 600 °C, almost all the carbon contamination corresponding to the C 1*s* XPS peak at $E - E_F = -286.1$ eV is removed. Additionally, the O 1*s* spectra undergo a big change after thermal treatment, which is reflected in its intensity as well as in the shape

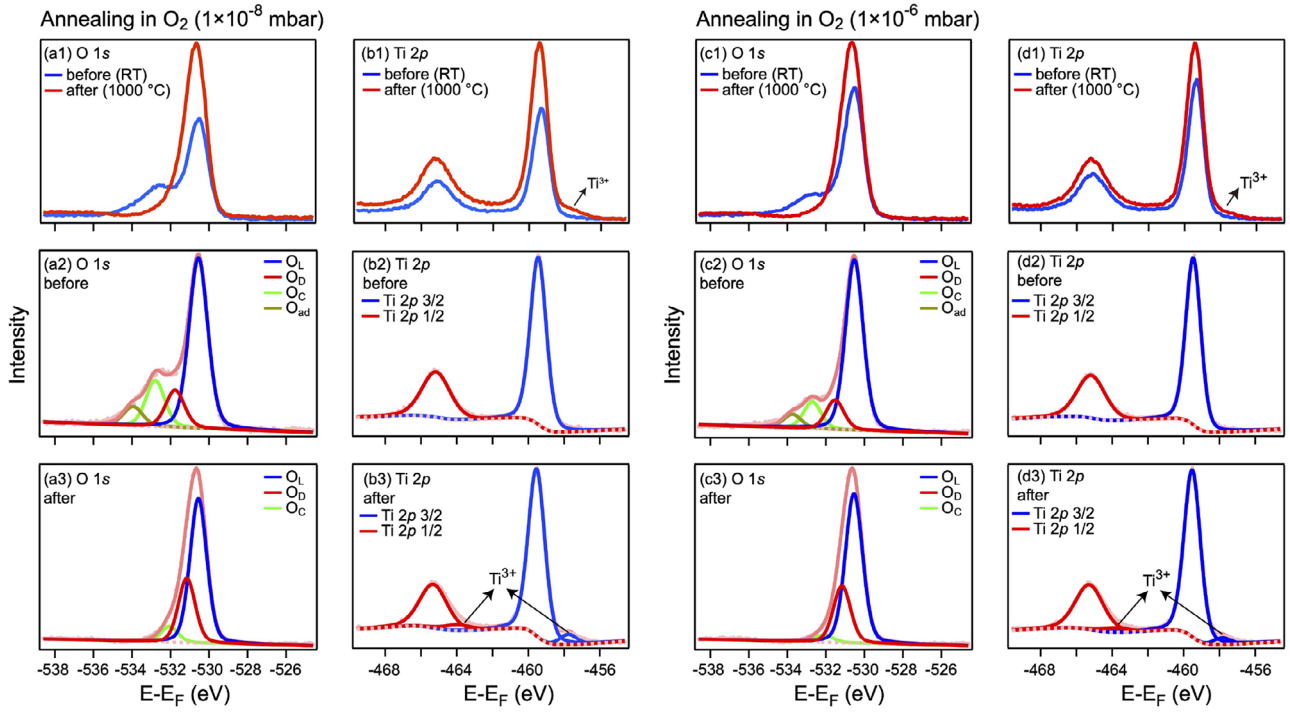

Figure 4. Core-level O 1s and Ti 2*p* XPS spectra (and the respective results of the fit routine) collected "before" and "after" in situ annealing of STO-TO eutectic samples at different partial pressures of O_2 (marked in the figure).

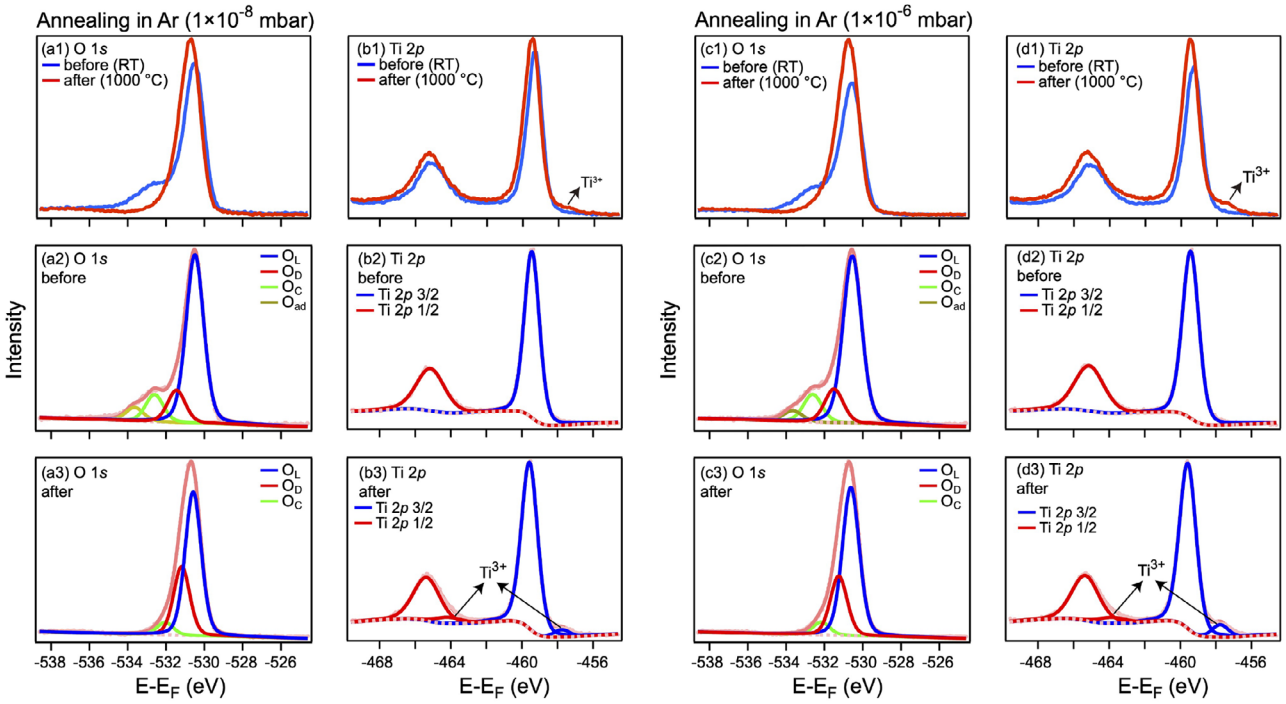

Figure 5. Core-level O 1*s* and Ti 2*p* XPS spectra (and the respective results of the fit routine) collected "before" and "after" in situ annealing of STO-TO eutectic samples at different partial pressures of Ar (marked in the figure).

of the peak. In Figure 4(a2),(c2), four emission lines at $E - E_F \approx -530.5$ eV, $E - E_F \approx -531.8$ eV, $E - E_F \approx -532.8$ eV, and $E - E_F \approx -533.9$ eV can be identified in the "before" XPS O 1*s* spectra which, can be assigned to the oxygen atoms in the lattice (O_L), oxygen defects (O_D), C–O bond (O_C) in the bulk sample, and the adsorbed water (O_{ad}), respectively.[42,44] Due to the in situ thermal treatment, the components associated with O–H bonds disappear from the spectra (see "after" in Figure 4(a3,c3)). At the same time, the intensities of XPS components associated with O_D and O_C demonstrate a significant growth and a strong reduction, respectively. For the Ti 2*p* spectra (Figure 4(b1–b3,d1–d3), the strong increase of the intensity "after" thermal annealing is due to the cleaning of the STO-TO sample's surface. In addition, a shoulder peak which can be assigned to the Ti^{3+} state appeared in the spectra, that could be due to the increase of the number of oxygen defects "after" thermal annealing (see also Figures S2 and S3, Supporting Information).

The respective percentage ratio of the peak intensities O_D/O_L for the stepwise annealing of STO-TO in O_2 at 1×10^{-8} and 1×10^{-6} mbar are summarized in **Table 3**. The observed trend suggests that the O_D/O_C ratio slightly decreases after the start of annealing steps (at 250 °C) in UHV and at "low-pressure" O_2 treatment. This may be caused by the complete removal of the O–H groups from the surface and the decrease of the spectral intensity associated with the C–O bonds. Moreover, we can find that 600° C is a key temperature for thermal annealing, and the slope of the O_D/O_C ratio is the highest in the whole annealing process. This means that the oxygen vacancies will start to form at this temperature very effectively. Then, with the increase of the annealing temperature to 800° C, the oxygen vacancies will increase continually. However, when the temperature reaches 1000° C, the concentration of the oxygen defects demonstrates a slow growth rate (see O_2, 1×10^{-8} mbar) or even decreases (see UHV and O_2, 1×10^{-6} mbar).

The similar XPS results, but for the thermal annealing of STO-TO samples in the presence of Ar at a partial pressure of 1×10^{-8} and 1×10^{-6} mbar are presented in Figure 5 (see also, Figures S4 and S5, Supporting Information). The same fitting components can be identified in the O 1*s* spectra associated with oxygen atoms in the lattice (O_L), oxygen defects (O_D), C–O bond (O_C) in the bulk sample, and the adsorbed water (O_{ad}), respectively. As before, the disappearance of the O_{ad} peak in Figure 5(a3,c3) for the O 1*s* spectra "after" annealing is due to the effective desorption of the water and hydroxyl surface contaminations. In case of the Ti 2*p* spectra (Figure 5(b1–b3),(d1–d3)) the corresponding Ti^{3+} shoulder peak can be observed "after" annealing, similar to the previously discussed result. Also, the similar evolution of the percentage ratio O_D/O_L is observed for the STO-TO sample annealed in situ in the presence of Ar as can be deduced from the results summarized in Table 3.

2.3.2. High-Pressure Treatment

Further XPS studies were performed for samples "before" and "after" thermal annealing at 1000 °C in the atmospheric-pressure flow of air, and pure O_2 and Ar gases. These results are compiled in Figure 6 and Figures S6 – S8 (Supporting Information), respectively. It can be noticed that the intensity of XPS lines for the STO-TO eutectic annealed in air and O_2 flow is significantly decreased compared with that of Ar. This may be assigned to the higher reactivity of STO-TO toward O_2 and air compared to that for Ar,

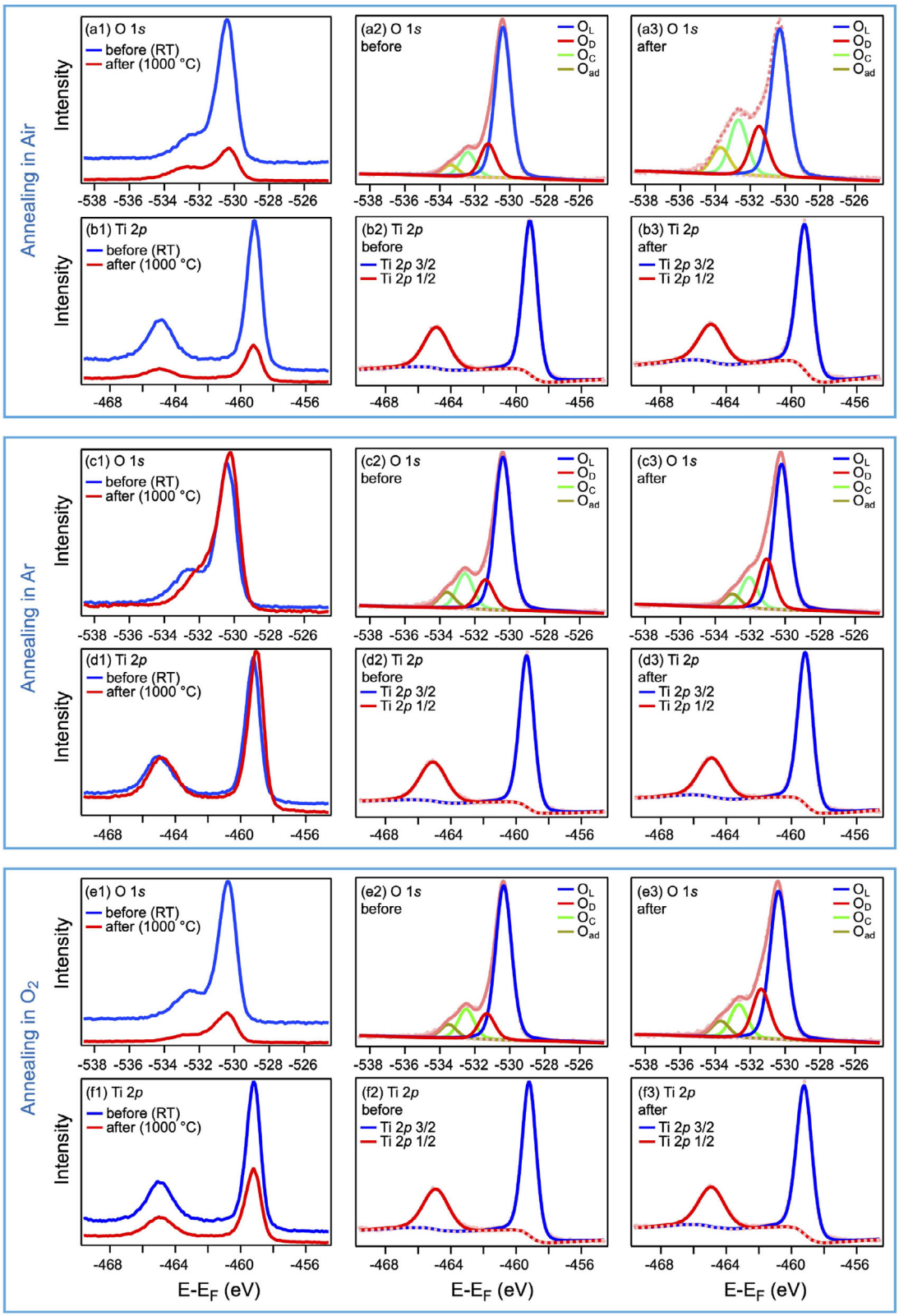

Figure 6. Core-level O 1*s* and Ti 2*p* XPS spectra (and the respective results of the fit routine) collected "before" and "after" ex situ annealing of STO-TO eutectic samples in flows of different gases (marked in the figure).

Table 3. The percentage ratios of O_D/O_L peak intensities extracted from fit of O 1*s* XPS spectra.

T [° C]	UHV	O_2 [1×10^{-8} mbar]	O_2 [1×10^{-6} mbar]	Ar [1×10^{-8} mbar]	Ar [1×10^{-6} mbar]	Air flow	Ar flow	O_2 flow
RT	16.28	21.8	17.21	19.08	20.11	22.32	19.38	16.78
250	14.29	17.05	15.48	18.14	15.08	/	/	/
400	25.28	22.43	21.43	21	22.82	/	/	/
600	42.25	31.56	39.11	43.33	29.15	/	/	/
800	51.79	35.82	46.47	38.6	47.34	/	/	/
1000	50.26	44.6	38.14	47.92	40.13	33.55	34.79	33.56

thus making the eutectic samples' surface less conductive. Another reason is that the atmospheric pressure of Ar in the reactor might prevent the evaporation of the "light" elements, like oxygen and Ti, at high temperature from the STO-TO sample, thus forcing them to remain in the sample. The similar effect was, e.g., observed during the preparation of high quality graphene layers on SiC under an atmospheric Ar environment, when Ar atoms prevent the fast inhomogeneous sublimation of Si atoms.[45]

Figure 6(a1–a3,c1–c3,e1–e3) shows the raw and fitted O 1*s* XPS spectra collected "before" thermal annealing in the flow of the gases, where four are peaks located at $E - E_F \approx -530.3$ eV, $E - E_F \approx -531.5$ eV, $E - E_F \approx -532.7$ eV, and $E - E_F \approx -533.7$ eV can be assigned to the oxygen atoms in the lattice (O_L), oxygen defect (O_D), C–O bond (O_C) in the bulk sample, and the adsorbed water (O_{ad}), respectively. In Table 3, O_D/O_L represents the relative increase in the number of oxygen vacancies. As can be seen from Table 3, the oxygen defects concentration in STO-TO eutectic remains almost the same after annealing in air and O_2 and is slightly lower compared to the STO-TO sample annealed in Ar flow. When annealing in an Ar stream, due to the lack of oxygen supply, the original oxygen inside the material may diffuse and escape to a certain extent at high temperatures, resulting in a relatively high concentration of oxygen defects. Comparison with the above presented results for the thermal annealing in UHV conditions using low partial pressures of gases shows that the high temperature annealing leads to the decreasing of the oxygen defects concentration in the STO-TO eutectic material. Low pressure reduces the resistance of oxygen atoms diffusing from the interior of the material to the external environment. In the low-pressure environment, the oxygen atoms inside the material are subject to less external pressure and are more likely to escape from the material. Additionally, the observation of the weak emission intensity of the Sr 3*d* XPS line in STO-TO samples after high temperature annealing (see Figures S6d, S7d and S8d, Supporting Information) is much in line with the above SEM/EDX and TEM/EDX results, confirming the evaporation of Sr from the surface of the studied samples.

Based on the above presented XPS, SEM/EDX, and TEM/EDX analysis, the evolution of oxygen vacancies and surface morphology in the $SrTiO_3$-TiO_2 eutectic during annealing can be rationalized in terms of thermally activated oxygen diffusion and atmosphere–dependent surface reactions. At elevated temperatures, lattice oxygen atoms possess sufficient mobility to escape from the crystal, producing oxygen vacancies that are accompanied by partial reduction of Ti^{4+} to Ti^{3+}. The balance between oxygen loss and replenishment depends strongly on the ambient gas atmosphere: under Ar or low-pressure O_2, the oxygen chemical potential is low, promoting vacancy formation, whereas under atmospheric-pressure O_2 or air, the increased reactivity of the surface can lead to the formation of volatile oxides (e.g., SrO_x or TiO_x), which explains the observed Sr depletion and surface roughening.

Furthermore, the TEM results indicate that high-temperature annealing enhances the crystallinity and sharpness of the $SrTiO_3/TiO_2$ interface. This behavior can be attributed to thermally induced atomic rearrangements and defect redistribution, which minimizes interfacial energy and favor phase separation. Such interface reconstruction, coupled with controlled oxygen vacancy concentration, is expected to improve charge transport and separation across the heterointerface, which is beneficial for the photocatalytic and photoelectrochemical applications of the STO-TO eutectic.

3. Conclusion

In summary, the studies of the influence of the in situ and ex situ thermal annealing, at different temperatures and in different gas atmospheres and pressures, on the electronic properties and structure of STO-TO eutectic materials were performed using different surface- and bulk-sensitive experimental methods. It was found that the oxygen defect concentration increased after annealing in all treatments. However, the different atmospheres show different inhibited effects on the final oxygen vacancy concentration, and the oxygen demonstrates the strongest inhibited effects during the low-pressure and high-pressure annealing process. Meanwhile, the experimental results demonstrate the existence of different "key temperatures" for the different gas atmospheres that the oxygen vacancy concentration increases below this "key temperature" and then decreases over this "key temperature," phenomenon which was previously reported in the literature.[46,47] More interestingly, our studies demonstrated that different annealing conditions correspond to different "key temperatures" and this finding can provide the experimental basis for the controllable tuning of oxygen vacancy concentration in STO-TO eutectic materials.

4. Experimental Section

The bulk STO-TO eutectic rod with a diameter of ≈3 mm was synthesized using the μ-pulling method from the mixture of $SrCO_3$ and TiO_2 (rutile and anatase phases) powders with a growth rate of 1 mm min^{-1} accord-

ing to the recipe published earlier in refs. [41, 42]. This rod was cut into several slices with a thickness of ≈0.5 − 1 mm and then polished from one side with a surface roughness below 100 nm. Before initial XPS analysis, the polished samples were ultrasonically cleaned using ethanol at 50 °C for 15 min. Thermal annealing of STO-TO samples was performed in different conditions: i) "low-pressure" treatment with stepwise increased annealing temperature from 250 to 1000 °C in UHV, O_2 and Ar (with a partial pressure of 1×10^{-8} and 1×10^{-6} mbar) environments; ii) "high-pressure" treatment at 1000 °C in Ar, O_2 and Ar flows using the quartz furnace. Annealing time in all steps was always 60 min.

Laboratory-based XPS characterization was performed in the UHV station installed at Shanghai University and consisting of preparation and analysis chambers with a base pressure better than 1×10^{-10} mbar (SPECS Surface Nano Analysis GmbH). XPS spectra were collected using a monochromatized Al *Kα* ($h\nu = 1486.6$ eV) X-ray source (emission angle $\phi = 30°$) and SPECS PHOIBOS 150 hemispherical analyzer combined with a 2D-CMOS detector. The X-ray source spot on the anode is 0.5×3.5 mm^2 in size (corresponds to 0.2×3.5 mm^2 on the sample). XPS spectra were measured with a pass energy of 50 eV for survey scans and 20 eV for high-resolution scans. It should be noted that the charge neutralizer was not used in the experiments reported herein. The calibration of the binding-energy scale as well as the Fermi level position are confirmed by examining the sputter–cleaned Ag samples. All data were analyzed using XPST (X-ray Photoelectron Spectroscopy Tools) program package for Igor Pro software. It includes various graphical interfaces and command-line functions to facilitate the processing of XPS data. The fitting process selects a Gaussian–Lorentzian mixed function (with a ratio of 70% Gaussian and 30% Lorentzian) for fitting.

SEM/EDX data were collected using the ZEISS SIGMA 500 microscope. HR-TEM measurements were performed using a FEI Talos F200x G2 instrument with EDX (super-X) and the FIB preparation was performed using an FEI Scios 2 HiVac. All EDX quantitative analyses were based on the K_α (for O and Ti) and L_α (for Sr) X-ray characteristic lines.

Supporting Information

Supporting Information is available from the Wiley Online Library or from the author.

Acknowledgements

The authors thank the National Natural Science Foundation of China (Grant No. 22272104) for financial support. Y.D. acknowledges the project Centre for Advanced Laser Techniques (CALT), co-funded by the European Union through the European Regional Development Fund under the Competitiveness and Cohesion Operational Programme (Grant No. KK.01.1.1.05.0001).

Open access publishing facilitated by Institut Ruder Boskovic, as part of the Wiley - National and University Library in Zagreb Consortium Croatian Academic and Research Libraries Consortium agreement.

Conflict of Interest

The authors declare no conflict of interest.

Data Availability Statement

The data that support the findings of this study are available from the corresponding author upon reasonable request.

Keywords

EDX, eutectic, SEM, semiconductor, TEM, XPS

Received: September 30, 2025
Revised: October 27, 2025
Published online:

[1] J. Li, H. Yuan, W. Zhang, B. Jin, Q. Feng, J. Huang, Z. Jiao, *Carbon Energy* **2022**, *4*, 294.
[2] S. Kim, K. H. Kim, C. Oh, K. Zhang, J. H. Park, *Carbon Energy* **2022**, *4*, 21.
[3] J. Schneider, M. Matsuoka, M. Takeuchi, J. Zhang, Y. Horiuchi, M. Anpo, D. W. Bahnemann, *Chem. Rev.* **2014**, *114*, 9919.
[4] M. Ge, Q. Li, C. Cao, J. Huang, S. Li, S. Zhang, Z. Chen, K. Zhang, S. S. Al-Deyab, Y. Lai, *Adv. Sci.* **2017**, *4*, 1600152.
[5] C. Avcioglu, S. Avcioglu, M. F. Bekheet, A. Gurlo, *ACS Appl. Energy Mater.* **2023**, *6*, 1134.
[6] C. B. Ong, L. Y. Ng, A. W. Mohammad, *Renew. Sustain. Energy Rev.* **2018**, *81*, 536.
[7] Z. Mirzaeifard, Z. Shariatinia, M. Jourshabani, S. M. R. Darvishi, *Ind. Eng. Chem. Res.* **2020**, *59*, 15894.
[8] C. Feng, Z. Wang, Y. Ma, Y. Zhang, L. Wang, Y. Bi, *Appl. Catal. B: Environ.* **2017**, *205*, 19.
[9] R. Yang, Y. Fan, Y. Zhang, L. Mei, R. Zhu, J. Qin, J. Hu, Z. Chen, Y. H. Ng, D. Voiry, S. Li, Q. Lu, Q. Wang, J. C. Yu, Z. Zeng, *Angew. Chem. Int. Ed.* **2023**, *62*, e202218016.
[10] Z. Cheng, T. A. Shifa, F. Wang, Y. Gao, P. He, K. Zhang, C. Jiang, Q. Liu, J. He, *Adv. Mater.* **2018**, *30*, 1707433.
[11] M. Zhu, H. Kou, K. Wang, H. Wu, D. Ding, G. Zhou, S. Ding, *Mater. Horiz.* **2020**, *7*, 3131.
[12] Y. Dedkov, Y. Guo, E. Voloshina, *Electron. Struct.* **2023**, *5*, 043001.
[13] J. Dai, K. Wang, E. Voloshina, Y. Dedkov, B. Paulus, *ACS Omega* **2023**, *8*, 33920.
[14] A. Fujishima, K. Honda, *Nature* **1972**, *238*, 37.
[15] A. Fujishima, X. Zhang, D. A. Tryk, *Surf. Sci. Rep.* **2008**, *63*, 515.
[16] K. Domen, S. Naito, M. Soma, T. Onishi, K. Tamaru, *J. Chem. Soc., Chem. Commun.* **1980**, *0*, 543.
[17] K. Domen, S. Naito, T. Onishi, K. Tamaru, M. Soma, *J. Phys. Chem.* **1982**, *86*, 3657.
[18] H. M. Zeeshan, S. Sharma, M. Panahi, E. Voloshina, Y. Dedkov, *Phys. Chem. Chem. Phys.* **2022**, *24*, 25720.
[19] S. G. Ullattil, S. B. Narendranath, S. C. Pillai, P. Periyat, *Chem. Eng. J.* **2018**, *343*, 708.
[20] J. Zhang, L. Zhang, Y. Shi, G. Xu, E. Zhang, H. Wang, Z. Kong, J. Xi, Z. Ji, *Appl. Surf. Sci.* **2017**, *420*, 839.
[21] N. T. Padmanabhan, N. Thomas, J. Louis, D. T. Mathew, P. Ganguly, H. John, S. C. Pillai, *Chemosphere* **2021**, *271*, 129506.
[22] S. Zhang, X. Zhang, Y. Sun, W. Zhou, W. Cao, D. Cheng, *Int. J. Hydrogen Energy* **2023**, *48*, 29996.
[23] A. Esrafili, M. Salimi, A. j. jafari, H. R. Sobhi, M. Gholami, R. R. Kalantary, *J. Mol. Liq.* **2022**, *352*, 118685.
[24] C. Xia, T. H. C. Nguyen, X. C. Nguyen, S. Y. Kim, D. L. T. Nguyen, P. Raizada, P. Singh, V.-H. Nguyen, C. C. Nguyen, V. C. Hoang, Q. V. Le, *Fuel* **2022**, *307*, 121745.
[25] Y. Guo, X. Fu, Y. Xie, L. Zhu, R. Liu, L. Liu, *Opt. Mater.* **2022**, *133*, 112980.
[26] J. Ran, J. Zhang, J. Yu, M. Jaroniec, S. Z. Qiao, *Chem. Soc. Rev.* **2014**, *43*, 7787.
[27] M. Rafique, S. Hajra, M. Irshad, M. Usman, M. Imran, M. A. Assiri, W. M. Ashraf, *ACS Omega* **2023**, *8*, 25640.
[28] Z. Jiang, K. Qian, C. Zhu, H. Sun, W. Wan, J. Xie, H. Li, P. K. Wong, S. Yuan, *Appl. Catal. B: Environ.* **2017**, *210*, 194.
[29] A. Sen, M. H. Putra, A. K. Biswas, A. K. Behera, A. Gross, *Dye. Pigment.* **2023**, *213*, 111087.

[30] X. Bi, G. Du, A. Kalam, D. Sun, Y. Yu, Q. Su, B. Xu, A. G. Al-Sehemi, *Chem. Eng. Sci.* **2021**, *234*, 116440.
[31] D. V. Christensen, M. v. Soosten, F. Trier, T. S. Jespersen, A. Smith, Y. Chen, N. Pryds, *Adv. Electron. Mater.* **2017**, *3*, 1700026.
[32] T. Malevu, B. Mwankemwa, S. Motloung, K. Tshabalala, R. Ocaya, *Phys. E: Low-Dimens. Syst. Nanostructures* **2019**, *106*, 127.
[33] Z. Xie, S. Shuang, L. Ma, F. Zhu, X. Liu, Z. Zhang, *RSC Adv.* **2017**, *7*, 51382.
[34] A. Janotti, J. B. Varley, P. Rinke, N. Umezawa, G. Kresse, C. G. V. d. Walle, *Phys. Rev. B* **2009**, *81*, 085212.
[35] E. Wahlstrom, E. K. Vestergaard, R. Schaub, A. Ronnau, M. Vestergaard, E. Laegsgaard, I. Stensgaard, F. Besenbacher, *Science* **2004**, *303*, 511.
[36] M. Meng, S. Zhou, L. Yang, Z. Gan, K. Liu, F. Tian, Y. Zhu, C. Li, W. Liu, H. Yuan, Y. Zhang, *Nanotechnology* **2018**, *29*, 155401.
[37] H. Wu, Z. Wang, S. Jin, X. Cao, F. Ren, L. Wu, Z. Xing, X. Wang, G. Cai, C. Jiang, *Int. J. Hydrogen Energy* **2018**, *43*, 6936.
[38] Y. Huang, Y. Yu, Y. Yu, B. Zhang, *Sol. RRL* **2020**, *4*, 2000037.
[39] J. Li, S. Zhang, J. Yang, X. Zheng, *Vacuum* **2021**, *194*, 110579.
[40] S. S. Rao, Y. F. Lee, J. T. Prater, A. I. Smirnov, J. Narayan, *Appl. Phys. Lett.* **2014**, *105*, 042403.
[41] K. Wysmulek, J. Sar, P. Osewski, K. Orlinski, K. Kolodziejak, A. Trenczek-Zajac, M. Radecka, D. A. Pawlak, *Appl. Catal. B* **2017**, *206*, 538.
[42] Y. Guo, H. M. Zeeshan, M. Yan, W. Qin, W. Yang, S. Cao, Y. Dedkov, E. Voloshina, *Adv. Energy Sustain. Res.* **2023**, *4*, 2300136.
[43] B. A. Pinaud, P. C. K. Vesborg, T. F. Jaramillo, *J. Phys. Chem. C* **2012**, *116*, 15918.
[44] F. Lei, Y. Sun, K. Liu, S. Gao, L. Liang, B. Pan, Y. Xie, *J. Am. Chem. Soc.* **2014**, *136*, 6826.
[45] K. V. Emtsev, A. Bostwick, K. Horn, J. Jobst, G. L. Kellogg, L. Ley, J. L. McChesney, T. Ohta, S. A. Reshanov, J. Röhrl, E. Rotenberg, A. K. Schmid, D. Waldmann, H. B. Weber, T. Seyller, *Nat. Mater.* **2009**, *8*, 203.
[46] P. Srilakshmi, M. Sivakumar, A. Kathirvel, A. U. Maheswari, *J. Nanoparticle Res.* **2021**, *23*, 224.
[47] C. Liu, R. Mao, Q. Wu, J. Li, D. Zheng, Z. Fei, C. Pang, *AIP Adv.* **2023**, *13*, 065217.